Biophysical Impact of Land Use and Land Cover Change on Subgrid Temperature in CMIP6 Models

Article *in* Journal of Hydrometeorology · October 2022

DOI: 10.1175/JHM-D-22-0073.1

7 authors, including:

Tao Tang
Yale University
10 PUBLICATIONS **99** CITATIONS
SEE PROFILE

Keer Zhang
Yale University
4 PUBLICATIONS **14** CITATIONS
SEE PROFILE

Lei Cai
Yunnan University
25 PUBLICATIONS **275** CITATIONS
SEE PROFILE

David Lawrence
Geisel School of Medicine at Dartmouth
292 PUBLICATIONS **43,638** CITATIONS
SEE PROFILE

Biophysical Impact of Land-Use and Land-Cover Change on Subgrid Temperature in CMIP6 Models

TAO TANG,[a] XUHUI LEE,[a] KEER ZHANG,[a] LEI CAI,[b,c] DAVID M. LAWRENCE,[d] AND ELENA SHEVLIAKOVA[e]

[a] *School of the Environment, Yale University, New Haven, Connecticut*
[b] *Norwegian Research Centre, Bergen, Norway*
[c] *Department of Atmospheric Sciences, Yunnan University, Kunming, China*
[d] *National Center for Atmospheric Research, Boulder, Colorado*
[e] *NOAA/Geophysical Fluid Dynamics Laboratory, Princeton, New Jersey*

(Manuscript received 13 April 2022, in final form 7 October 2022)

ABSTRACT: In this study, we investigate the air temperature response to land-use and land-cover change (LULCC; cropland expansion and deforestation) using subgrid land model output generated by a set of CMIP6 model simulations. Our study is motivated by the fact that ongoing land-use activities are occurring at local scales, typically significantly smaller than the resolvable scale of a grid cell in Earth system models. It aims to explore the potential for a multimodel approach to better characterize LULCC local climatic effects. On an annual scale, the CMIP6 models are in general agreement that croplands are warmer than primary and secondary land (psl; mainly forests, grasslands, and bare ground) in the tropics and cooler in the mid–high latitudes, except for one model. The transition from warming to cooling occurs at approximately 40°N. Although the surface heating potential, which combines albedo and latent heat flux effects, can explain reasonably well the zonal mean latitudinal subgrid temperature variations between crop and psl tiles in the historical simulations, it does not provide a good prediction on subgrid temperature for other land tile configurations (crop vs forest; grass vs forest) under Shared Socioeconomic Pathway 5–8.5 (SSP5–8.5) forcing scenarios. A subset of simulations with the CESM2 model reveals that latitudinal subgrid temperature variation is positively related to variation in net surface shortwave radiation and negatively related to variation in the surface energy redistribution factor, with a dominant role from the latter south of 30°N. We suggest that this emergent relationship can be used to benchmark the performance of land surface parameterizations and for prediction of local temperature response to LULCC.

KEYWORDS: Atmosphere; Land surface; Boundary currents; Climate models

1. Introduction

Land-use activities contribute to climate change via biogeochemical and biophysical effects (e.g., Bonan 2008; Lee et al. 2011; Boysen et al. 2020). The former is associated with the release of carbon to the atmosphere, lifting atmospheric CO_2 concentration (e.g., Pan et al. 2011), while the latter is related to the change of surface properties (e.g., albedo and roughness) and latent heat (LE) flux (e.g., Davin and de Noblet-Ducoudré 2010; Li et al. 2015). Traditionally, modeling investigations of land-use and land-cover change (LULCC) are conducted by running two sets of Earth system model (ESM) simulations: the first with preindustrial land-cover distributions and the second with a present-day or a prescribed future land-cover map. One difficulty with this modeling strategy is how to properly disentangle LULCC climate signals from unforced model variability and nonlocal feedback effects via changes to atmospheric and oceanic circulations (Pitman et al. 2009; Pielke et al. 2011; Chen and Dirmeyer 2020). It is possible to better characterize the variability and enlarge the signal-to-noise ratio by performing a large number of perturbation and control simulations, but the computing cost is prohibitive.

An alternative approach detects the biophysical effects of LULCC in "all-forcing" modeling experiments (Kumar et al. 2013; Lejeune et al. 2017) using a space-for-time substitution (Lee et al. 2011). It searches iteratively for grid cells affected and neighboring grid cells unaffected by LULCC. The temperature and energy flux contrasts between these two groups of grid cells are regarded as the climatic signal of LULCC. This method has been used successfully in the investigation of regional LULCC effects (Li et al. 2016b).

A third approach uses a chessboard method to investigate deforestation climate effects (Winckler et al. 2017; Prevedello et al. 2019; Robertson 2019). In these studies, deforested grid cells are scattered in a chessboard pattern across the globe. Model simulation is performed only once. The deforestation signal is obtained by comparing deforested grid cells with neighboring forested grid cells in the same model run. The space-for-time analogy is tacitly assumed in data interpretation. This method provides more spatially refined insights than the other two methods. Common to all the three methods is that results are reported as gridcell means.

In this study, we investigate the climate effects of LULCC by evaluating model output at the subgrid-scale, following Malyshev et al. (2015) and others. One reason for doing this is

Supplemental information related to this paper is available at the Journals Online website: https://doi.org/10.1175/JHM-D-22-0073.s1.

Corresponding author: Tao Tang, tao.tang@yale.edu

DOI: 10.1175/JHM-D-22-0073.1

that ongoing land-use activities are occurring at local scales that are typically smaller than the resolvable scale of a grid cell in ESMs (on the order of 100 km). ESMs typically represent land surface heterogeneity by dividing land grid cells into subgrid tiles, with each tile having similar physical, ecological, and biogeochemical characteristics (Malyshev et al. 2015; Lawrence et al. 2016; Lawrence et al. 2019). Generally, each tile within a grid cell receives the same forcing from the atmosphere, including incoming solar radiation, incoming longwave radiation, precipitation, temperature, humidity, and wind at the first model grid height, but the biophysical and biogeochemical state and flux variables are simulated at each subgrid level and then aggregated to produce grid-averaged values that are passed back to the atmosphere. Since the same atmospheric forcing is applied to all subgrid tiles within the same grid cell, the differing responses of land-cover types to the same atmospheric conditions can be examined (Malyshev et al. 2015). By focusing on subgrid variations, it may be possible to generate process-level information at the scales at which land-use activities—urbanization, deforestation, afforestation, agricultural intensification, and other land management—are occurring. An additional benefit is that the geographical region of study is not limited solely to regions that have undergone large-scale land-use transitions. Instead, this method can be used to quantify potential impacts of proposed land-use changes virtually anywhere on the globe, as long as multiple land-use types exist within a single grid cell.

So far, subgrid data have been used in quantification of and adaptation to urban heat stress using data from urban tiles (Zhao et al. 2014; Oleson et al. 2015; Li et al. 2016), projection of global lake evaporation changes using data from lake tiles (Wang et al. 2018), evaluation of deforestation on local surface climate using forest and grass plant functional types (PFTs) (Schultz et al. 2016; Liao et al. 2020), assessment of vulnerability of food production to climate change using subgrid data generated for crop tiles (Ren et al. 2018), evaluation of land-atmosphere parameterizations (Hao et al. 2022), and effects of nitrogen deposition on LULCC-modified lands (Paulot et al. 2018). These studies have revealed the dominant roles of albedo and LE in controlling subgrid temperature variations, in agreement with observed deforestation effects (da Rocha et al. 2004; von Randow et al. 2004) and with model simulations of large-scale deforestation (Bonan 2008; Li et al. 2016b). Specifically, in low latitudes, open land (e.g., cropland and grassland) is warmer than forests because of reduced LE. In mid–high-latitude regions, the pattern is reversed because open land has higher albedo than forests. A reduction of LE through transpiration and an increase in sensible heat flux was identified as a primary cause for the summertime northern midlatitude temperature response to cropland expansion (Findell et al. 2017). Li et al. (2016a) proposed that the combined effect of albedo and LE can be predicted by the heating potential difference between land-use types, as

$$\Delta H_p = \Delta\text{netSW} - \Delta\text{LE}, \tag{1}$$

where H_p (= netSW − LE) denotes heating potential, netSW is net shortwave radiation at the surface, and Δ denotes difference between two land-use types. The H_p difference can explain reasonably well the latitudinal dependence of satellite-observed surface temperature (skin temperature) contrast between forests and grasslands (Schultz et al. 2017).

Understanding how air temperature responds to LULCC is highly relevant to human and ecological health. It is not known if ΔH_p has the same predictive power for 2-m air temperature variations between forests and grasslands or for variations between other land-use types (e.g., forest vs cropland). One concern is that the LULCC climate effect is also controlled by the efficiency of energy redistribution between the surface and the atmospheric boundary layer. In a future CO_2-enriched world, the stomatal conductance of land ecosystems is projected to decrease (Yang et al. 2019), leading to decreased efficiency of turbulent flux and therefore may enlarge subgrid variations in temperature. Even though crops and grasses are both considered open land [with low surface roughness, similar albedos and relatively low leaf area index (LAI)], cropland expansion (at the expense of primary and secondary land) is known to cause different temperature responses than replacement of forests by grasslands (Bonan 2001), partly because of the differences in seasonal LAI patterns and greenness (Lamchin et al. 2020).

Multimodel approaches have become a central component to national and international assessments to understand past, present and future climates (Taylor et al. 2012; Eyring et al. 2016; Jia et al. 2019). To date, published studies on subgrid-scale temperature responses to LULCC have relied on one or at most two models (Malyshev et al. 2015; Schultz et al. 2016; Liao et al. 2020), and no attempt has been made to evaluate the subgrid-scale temperature response using a multimodel ensemble. A multimodel approach has the potential to obtain a more robust estimate of the climate effects of LULCC, including a range of projected outcomes and the drivers of these outcomes, and also may uncover limitations in land parameterization schemes.

In this study, we analyzed the subgrid results from seven simulations produced by four CMIP6 models. These simulations were conducted under three CO_2 forcing scenarios [historical, Shared Socioeconomic Pathway 5–8.5 (SSP5–8.5), and $4 \times CO_2$]. We focus on three types of subgrid variations [crop vs primary and secondary land (psl), grass vs forest, and crop vs forest] across latitudes. By examining latitudinal patterns of subgrid screen-height (2 m) air temperature response and model-to-model variations, we hope to generate insights that can help to improve LSM performance. Another specific goal is to evaluate if heating potential can form an emergent relationship on the subgrid temperature response to LULCC in this ensemble of model simulations. Process-based emergent relationships, established with multimodel ensembles and constrained by observations, have been shown to enable credible projections on many other aspects of the climate system, such as the snow albedo and the carbon cycle feedback (Hall et al. 2019). A robust emergent relationship for subgrid surface climate may improve our ability to predict the climate effect of local LULCC.

2. Model descriptions and simulations

The historical climate simulations were made with four ESMs: CESM2, NorESM2-LM, GFDL-ESM4, and UKESM1-0-LL.

TABLE 1. Models and simulations used in this study.

Model	Resolution (lat × lon)	Land surface model	Soil configuration	Forcing	Tile pair	Irrigation	Reference
NCAR-CESM2 (default)	0.9 × 1.25	CLM5	Shared	Hist-noLu	Crop–psl	On	Lawrence et al. (2019), Danabasoglu et al. (2020)
NorESM22-LM	1.9 × 2.5	CLM5	Shared	Hist-noLu	Crop–psl	On	Seland et al. (2020)
GFDL-ESM4	1.0 × 1.25	LM4	Individual	Hist-noLu	Crop–psl	Off	Zhao et al. (2018), Dunne et al. (2020)
UKESM11-0-LL	1.25 × 1.9	JULES-GL7.0	Shared	Hist-noLu	Crop–psl	Off	Sellar et al. (2019), Wiltshire et al. (2020)
NCAR-CESM2 (individual soil)	0.9 × 1.25	CLM5	Individual	Hist-noLu	Crop–psl	On	Schultz et al. (2016)
NCAR-CESM2 (individual soil)	0.9 × 1.25	CLM5	Individual	4 × CO_2	Crop–psl	Off	This study
NCAR-CESM2 (individual soil)	0.9 × 1.25	CLM5	Individual	SSP5-8.5	Crop–forest Grass–forest	On	Zhang et al. (2022)

These models are participants of the Land Use Model Intercomparison Project (LUMIP) (Lawrence et al. 2016). LUMIP is one the 21 endorsed MIPs under the CMIP6 protocol (Eyring et al. 2016), with the aim to advance our understanding of the impacts of LULCC on the climate and the biogeochemical cycle. The experiment employed in this study, labeled "hist-noLu," was forced by anthropogenic and natural forcing from 1850 to 2014, while the land use and land cover were held constant at the year of 1850. In other words, the fraction of cropland and pastureland, the crop type distribution, land management regimes, wood harvesting, fire ignition/suppression rates, and so on, did not vary during the simulation period. In CESM2, vegetation structure (LAI, stem area index, canopy top and bottom heights) were calculated prognostically with its BGC model. The basic configurations of these models and their LSM schemes are summarized in Table 1.

We performed one extra hist-noLu simulation using CESM2 with a modified version of its land scheme. In CLM5, the land component of CESM2 (Lawrence et al. 2019), the land surface is represented as a nested hierarchy of subgrid levels. The first subgrid level is the land unit, including vegetation, lake, urban, glaciers, and crops, with a fraction assigned to each land unit. The crop tile contains managed, unmanaged, rainfed and irrigated crops. The irrigation option is enabled in both hist-noLu simulations. In irrigated croplands, a check is made once per day to determine whether irrigation is required on that day. Irrigation is required if crop leaf area is positive and the available soil water is below a specific threshold (Lawrence et al. 2018). The second subgrid level is the column, which intends to capture variability in the soil and snow state variables within a single land unit. The key characteristic of the column level is that this is where the state variables for water and energy in the soil and snow are defined. The third subgrid level is PFT, which captures the biophysical and biogeochemical differences between broad categories of plants. In the default CLM5 configuration, the vegetated land unit is assigned a single column whereby all the PFTs in the unit share the same soil column in terms of water, nutrient use and soil heat exchange. Recent studies have shown that this shared soil column configuration can lead to unrealistic ground heat fluxes because a common soil temperature is artificially maintained for all PFTs within a column (Schultz et al. 2016; Meier et al. 2018). In this new hist-noLu simulation, each PFT in the vegetation unit was assigned its own soil column, following the method described by Schultz et al. (2016). We note that UKESM1 and NorESM2 are configured with shared soil column and GFDL has an individual soil column for different vegetation and land-use types (Table 1).

Although CESM2-CLM5.0 (and presumably the other models) can output data at the PFT level, the LUMIP protocol only requested subgrid data for up to four subgrid tiles (psl, crop, urban, and pastureland), and only two tiles (psl and crop) have complete data across the four LUMIP models assessed here. For this reason, our multimodel analysis is restricted to subgrid variations between these two tiles. In LUMIP, the psl tile is an area-weighted aggregation of forest, unmanaged grassland, and shrub.

The NorESM2 model uses CLM5 as its land component (Seland et al. 2020). All vegetation PFTs share a single soil column.

The land component of the GFDL model, LM4, is based on the LM3 model (Shevliakova et al. 2009; Zhao et al. 2018). In LM4, each grid cell consists of up to 15 tiles (including a bare soil tile) to represent subgrid differences in hydrology and carbon states. Each tile has its own soil column. Changes in tile types and areas occur annually according to the Land-Use Harmonization dataset (Hurtt et al. 2020). The physical and biogeochemical fluxes between the land and the atmosphere are calculated separately for each tile. There is no real crop in the GFDL model; instead, cropland is approximated by C_3 and C_4 grass (Shevliakova et al. 2009). For LUMIP subgrid tile reporting, all secondary and natural tiles are aggregated into the psl tile (Lawrence et al. 2016). Croplands are unirrigated.

The land component of UKESM1 model, JULES-GL7, uses a surface tiling scheme to represent subgrid heterogeneity. Tiles in a grid cell share a single soil column. Each tile has

its own albedo, surface conductance, turbulent fluxes, ground heat flux, radiation fluxes, snow mass and snow melt, and surface temperature. There are nine surface tiles consisting of five PFTs (broadleaf trees, needleleaf trees, C_3 grass, C_4 grass and shrubs) and four nonvegetated surface types (urban, inland water, bare soil, and ice). The tile fractions are spatially varying and produced by a remapping of the 17 IGBP types. The crop and pasture are physiologically identical to the natural grasses. For example, a cropland tile consists of 75% C_3 grass, 5% C_4 grass and 20% bare soil (Wiltshire et al. 2020). Irrigation in the UKESM1 is turned off in the CMIP6 simulations.

The spatial distribution of psl and crop fractions are shown in Fig. S1 in the online supplemental material. The psl tile takes up over 50% of the land surface in all models. The differences across the models are due to different treatments of the psl tile. For example, desert (bare ground) is included in psl tile of CESM2 and GFDL model, but not in UKESM1.

To investigate how atmospheric CO_2 influences subgrid temperature variations and to increase the number of subgrid tile configurations, we performed two more simulations with CESM2 using the individual soil column setup (Table 1). The first simulation was an instant quadrupling of the preindustrial CO_2 concentration ($4 \times CO_2$) with the same land use and land cover as in hist-noLu. This simulation was run in coupled mode for 120 years. Subgrid data were aggregated to four land tiles according to the LUMIP protocol and only the psl and the crop data were analyzed here. The second simulation was forced by the SSP5–8.5 scenario from 2015 to 2100. This is a high emission transient scenario, with atmospheric CO_2 increasing from about 400 ppm in 2015 to about 1135 ppm in 2100 resulting in a radiative forcing of 8.5 W m^{-2} in 2100 relative to the preindustrial level (Meinshausen et al. 2020). Atmospheric CO_2 can impact the surface climate directly via stomatal control on transpiration and indirectly via snow phenology change induced by changes in temperature. The multiple CO_2 scenarios allow us to determine which impact is stronger. The land use of year 2015 was used throughout the simulation. Subgrid data were archived for eight land tiles (Zhang et al. 2022). In this study, we analyzed the data for forest, crop, and grass tiles.

Some ESMs deploy a land parameterization that considers subgrid topographic effects (Tesfa and Leung 2017; Hao et al. 2022). In the ESMs shown in Table 1, there is no elevation change between different land uses within the same model grid.

3. Data analysis

The 2-m air temperature (T) variations are the main focus in this study. These variations were quantified as the difference, denoted by Δ, in T between three pairs of subgrid tiles, including 1) crop versus psl from the hist-noLu simulations and the $4 \times CO_2$ simulation, 2) crop versus forest from the SSP5-8.5 simulation, and 3) grass versus forest from the SSP5–8.5 simulation. In these paired calculations, psl and forest tiles are the baseline land use, and crop and grass are the perturbations. For example, when examining the data from hist-noLu simulations, ΔT is the difference in the 2-m air temperature between crop and psl (crop minus psl). The Δ values of other subgrid variables were calculated similarly (crop minus forest and grass minus forest). Unless stated otherwise, results are presented as seasonal and annual means of the last 20 years of each simulation. They are year 1995–2014 for the hist-noLu simulations, year 100–120 for the $4 \times CO_2$ simulation and 2081–2100 for the SSP5–8.5 simulation.

Using the space-for-time substitution, the contrast in temperature between the crop and the psl or forest tile can be regarded as the local climate effect of agricultural expansion. Likewise, the contrast between the grass and the forest tile is equivalent to the local climate effect of deforestation. This approach considers direct impact only. It does not include indirect impact due to atmospheric changes (e.g., cloud feedback) or effects of local terrain variations (Hao et al. 2022).

The subgrid temperature variations are related to subgrid variations in H_p, which were calculated according to Eq. (1). Subgrid variations in several biophysical properties and surface fluxes, including LAI, netSW, and LE, were also examined.

For a subset of model simulations, we investigated the dependence of ΔT on the efficiency of energy redistribution between each land tile and the overlaying atmosphere. This efficiency was quantified using the dimensionless energy redistribution factor f. Following Lee et al. (2011) and Bright et al. (2017), f was calculated from the diagnostic equation:

$$f = \frac{\lambda}{T_s - T_b}(R_n^* - G) - 1, \tag{2}$$

where T_s and T_b represent surface temperature and air temperature at the blending height (or the lowest atmospheric grid), respectively, λ is the local climate sensitivity given by $1/(4\sigma T_S^3)$ with σ being the Stefan–Boltzmann constant, G denotes the ground heat flux, and R_n^* is apparent net radiation given as

$$R_n^* = \downarrow\mathrm{SW} - \uparrow\mathrm{SW} + \downarrow\mathrm{LW} - \sigma T_b^4, \tag{3}$$

where $\downarrow$SW is the incoming shortwave radiation, $\uparrow$SW is the outgoing shortwave radiation, and $\downarrow$LW is the incoming longwave radiation. Higher f values indicate more efficient convection exchange or energy dissipation from the surface to the lower boundary layer. The daytime f ranges from about 2 to 30 and the nighttime f from about 0.3 to 4 (Chakraborty and Lee 2019). Calculation of f was made for three simulations, all using CESM2 (hist-noLu with independent soil column, $4 \times CO_2$, and SSP5–8.5) but was not done for other simulations because the blend-height air temperature was not available.

4. Results

a. *Climatic effects of cropland expansion: Geographic pattern*

Figure 1 maps the differences of annual mean temperature and H_p terms between crop and psl tiles for each model. In

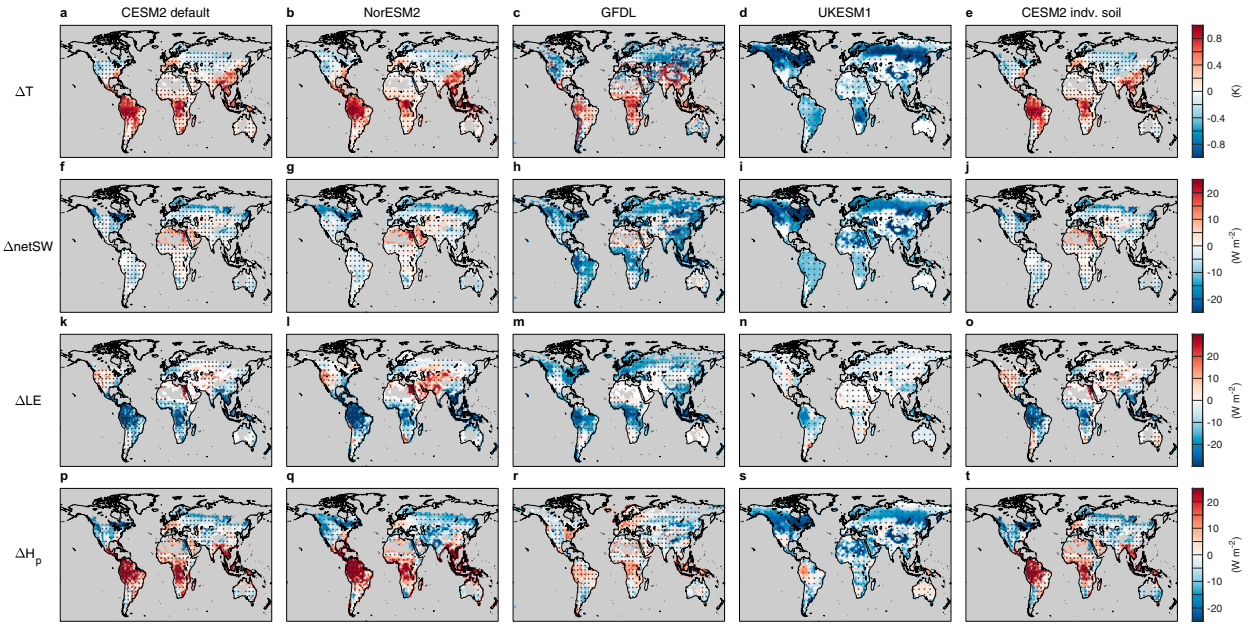

FIG. 1. Changes of annual mean temperature and heating potential terms for each model (crop minus psl). (a)–(e) Temperature T, (f)–(j) net SW radiation, (k)–(o) LE, and (p)–(t) heating potential H_p. Gray dots indicate that the changes are significant at 0.05 level based a two-sided Student's t test. The dots are shown every 5 grids for clarity.

the space-for-time framework, these subgrid variations can be interpreted as local climatic effects of cropland expansion. Cropland-induced cooling ($\Delta T < 0$) in mid–high latitudes of Northern Hemisphere (NH) and warming in the tropics ($\Delta T > 0$) are observed in all models with varying magnitudes, except for UKESM1. The UKESM1 model, on the other hand, shows a widespread cooling across the globe. The ΔT patterns are broadly consistent with previous studies using remote sensing data (Li et al. 2015, 2016a; Duveiller et al. 2018; Boysen et al. 2020) and can be largely explained by ΔH_p (Figs. 1p–t), in which grids with positive ΔH_p generally show positive ΔT, and vice versa. The spatial correlation coefficient r between ΔT and ΔH_p is higher than 0.74 ($p < 0.001$) except for GFDL model with $r = 0.23$ ($p < 0.001$). The result for GFDL is noisy compared with the CLM-based models.

On the whole, cropland expansion leads to a widespread decrease of net SW radiation, with a stronger drop in high latitudes, which is a result of an increase in albedo (Figs. 1f–j). There are two reasons for the difference: (i) In the growing season, croplands generally have a higher albedo than forests and therefore reflect more SW radiation (Pielke et al. 2011; Li et al. 2015; Duveiller et al. 2018); (ii) during the winter, snow can mask croplands but has smaller impact on forests, leading to a larger albedo effect at high latitudes (Robinson and Kukla 1984).

In all the models, cropland expansion results in a reduction of LE at low latitudes (ΔLE < 0, Figs. 1k–o), possibly owing to the shallower root system and smaller LAI of cropland compared with psl (Bonan 2008; Davin and de Noblet-Ducoudré 2010; Lawrence and Vandecar 2015), and reduced surface roughness (Winckler et al. 2019b). These models are not consistent in some midlatitude regions: ΔLE shows no change or slightly positive changes in arid zones (west North America and central Asia) in CLM-based models (two CESM2 simulations and one NorESM2 simulation) while in GFDL and UKESM1, ΔLE shows slightly negative values. Different model parameters such as root distribution and plant water uptake (Meier et al. 2018), as well as the differing responses of precipitation and snowfall (Li et al. 2015) may partially explain the incongruent responses of LE across the models.

b. Seasonal pattern of cropland climate effects

Figure 2 shows the seasonal evolution of zonal mean values for ΔT, ΔnetSW, and ΔLE between crop and psl tiles. Crops are warmer all year round (except for UKESM1, which produces cooling), with a slightly stronger warming in summer in CLM-based models than in GFDL in the tropics (Fig. 2, upper row). Such a warming pattern is mainly contributed by reduced LE (Fig. 2, lower row). The ΔT in mid–high latitudes (e.g., around 60°N) shows strong seasonality in all the models, with the strongest negative ΔT observed in February to May (Fig. 2, upper and middle rows), which is mainly attributed to the snow-masking effect (Bonan et al. 1992).

In the three CLM-based model simulations, there is a stripe of negative ΔT in the middle latitudes of NH in the spring-to-summer transition (from April to June; Figs. 2a,b,e). This cooling is mainly attributed to the positive ΔLE (Figs. 2k,l,o). The enhanced LE appears to be a result of the crop growth in the springtime as evidenced by positive ΔLAI (Fig. 3).

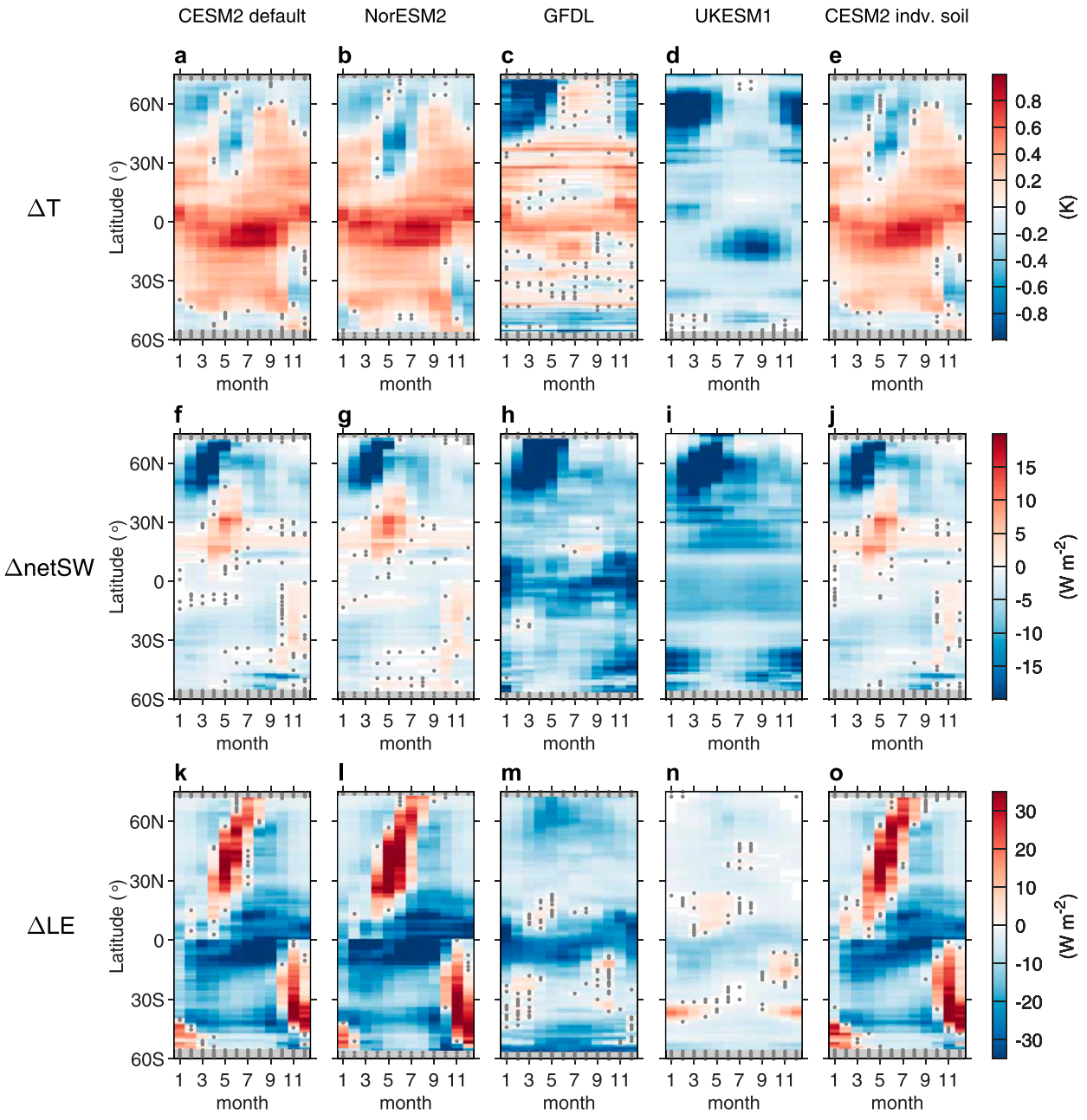

FIG. 2. Hovmöller plot for (a)–(e) ΔT, (f)–(j) ΔnetSW, and (k)–(o) ΔLE. Results shown are zonal mean values vs month. All results are crop minus psl. Gray dots indicate missing data or insignificant changes at the 0.05 level based on a two-sided Student's t test.

c. *Sensitivity to soil column configuration*

The three CLM-based model simulations show nearly identical zonal mean patterns of the subgrid contrasts in annual mean temperature and the H_p terms between crop and psl tiles (Figs. 4a,b,e). All show the largest drop in temperature around 60°N, with a zonal mean value from −0.24 to −0.28 K. Then ΔT increases southward and switches to positive values around 42°N, with a peak (0.61–0.71 K) in the tropical regions. The tropical (20°S–20°N) mean ΔT is 0.44 K (CESM2 default), 0.44 K (NorESM2), and 0.39 K (CESM2 individual soil; Fig. 5). The mean ΔT for mid–high latitudes (40°–70°N) is −0.07 K (CESM2 default), −0.09 K (NorESM2), and −0.11 K (CESM2 individual soil). In the CESM2 default and the NorESM2 simulations, all natural PFTs shared the same soil column, whereas in the CESM2 individual soil simulation, each PFT was assigned its own soil column. In all three simulations, crops had their own separate soil columns. Figures 4 and 5 indicate that the result for the psl tile is insensitive to soil column configuration.

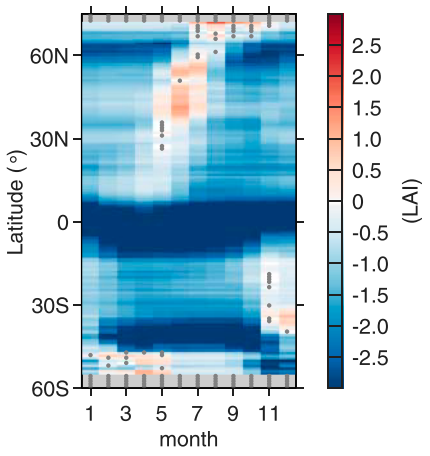

FIG. 3. As in Fig. 2, but for ΔLAI in the CESM2 model default simulation. Gray dots indicate missing data or insignificant changes at the 0.05 level based on a two-sided Student's *t* test.

Individual soil configuration is preferred over shared column configuration if the interest is subgrid variations between PFTs within the natural vegetation land unit, such as variations between forest and grass (Schultz et al. 2016). In the present study, the psl tile is an aggregate of multiple PFTs (forest, grass, shrub, and bare ground). The insensitivity shown in Figs. 4 and 5 indicates that the aggregation has mostly eliminated bias errors associated with unrealistic ground heat fluxes in shared column configuration.

d. *Influence of atmospheric CO_2 on subgrid variations*

Our model ensemble encompasses a wide range of CO_2 levels: from 285 to 400 ppm under the historical forcing, 1140 ppm in the 4 × CO_2 scenario and from 400 to 1135 ppm under the SSP5–8.5 scenario. To examine the influence of CO_2 on subgrid variations, we compare in Fig. 6 the zonal mean contrasts (crop minus forest) in T, netSW, and LE between the first 20 (2015–34) and the last 20 years (2081–2100) of the CESM2 model simulation under SSP5–8.5 scenario. The mean CO_2 concentration is ~430 ppm in the first period and ~1000 ppm in the last period. The grid by grid scatterplots are given in Fig. S2. The differences between these two periods can be explained by changing background climate and indirect effects of rising CO_2. For example, the magnitude of albedo effect may be reduced in a warmer world (Fig. 6b). A higher CO_2 concentration may reduce stomatal opening, resulting in a lower LE flux. The contrast in the ΔnetSW (crop minus forest) is less negative at mid–high latitudes in the second period than in the first period (Fig. 6b) because of less snowfall and a shorter snow cover duration in a warmer climate (Fig. S3), which leads to less negative ΔT in the high latitudes (Fig. 6a). The ΔLE is slightly more positive in the second than in the first period, due to more cropland irrigation (higher soil moisture content) driven by higher temperature in the later period (Fig. 6c). The CO_2 effect via stomatal regulation appears negligible on the differences between crops and forests.

e. *Emergent relationship on subgrid temperature variations*

Figure 7 shows the correlation between zonally averaged ΔT, ΔnetSW, ΔLE, and ΔH_p for crops minus psl. The correlation between ΔT and ΔnetSW is stronger for the mid–high latitudes than for the tropical regions, with a correlation coefficient of 0.86 ($p < 0.01$) and a slope of 0.04 K $(\mathrm{W\ m^{-2}})^{-1}$ across all models (Fig. 7a). This regional difference indicates a stronger albedo effect in the mid–high latitudes than in low

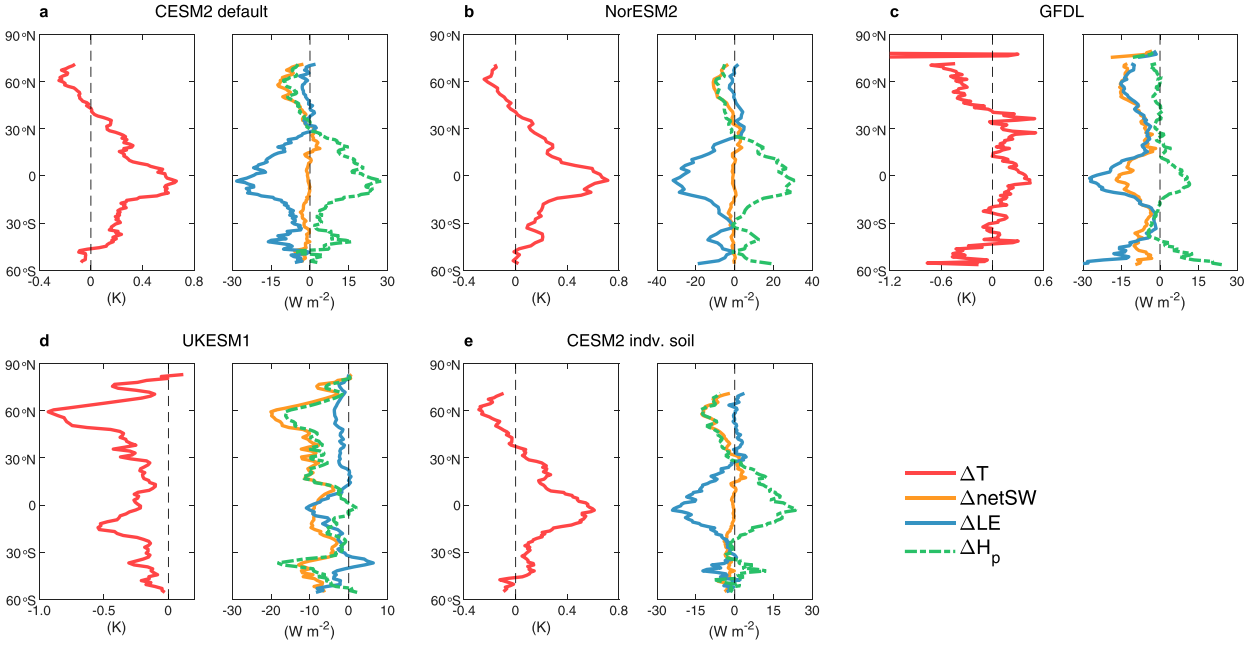

FIG. 4. Zonal mean changes (crop minus psl) of annual mean temperature and heating potential H_p terms for each model simulation.

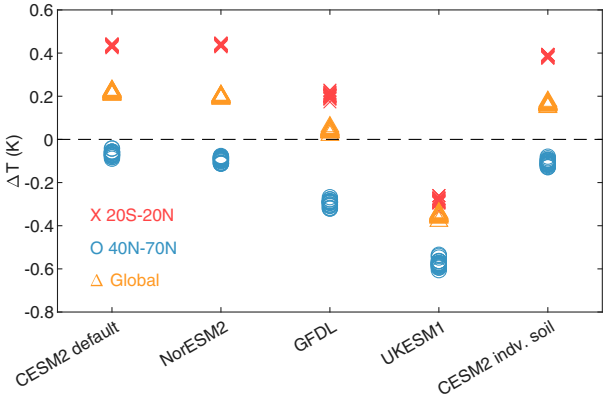

FIG. 5. Domain-averaged annual mean ΔT for tropical regions (red), mid–high-latitude regions (blue), and global land grids (orange, no Antarctica) for each model. Results are crop minus psl. Each circle represents a 1-yr value during 1995–2014.

latitudes. In contrast, ΔLE controls the temperature change in the tropical regions, characterized with a correlation coefficient of -0.80 ($p < 0.01$) and a slope of -0.03 K $(\text{W m}^{-2})^{-1}$ (Fig. 7b, red). The impact of ΔLE in the mid–high latitudes is relatively minor (Fig. 7b, blue). The correlation pattern with the heating potential ΔH_p does not differ much between the two zones (Fig. 7c).

The crop-versus-psl difference in the overall heating potential ΔH_p, which combines both ΔnetSW and ΔLE [Eq. (1)], as the independent variable correlates reasonably well with ΔT ($r = 0.72$, $p < 0.01$) for all latitudes and all hist-noLu model simulations (Fig. 7d). The regression equation is given by

$$\Delta T = -0.030 + 0.025\Delta H_p, \quad (4)$$

where ΔT is in kelvins and ΔH_p is in watts per square meter. In comparison, ΔT and ΔH_p in a large-scale deforestation experiment are highly correlated in the latitude zone from 20°S to 50°N but poorly correlated north of 50°N (Li et al. 2016a). A small group of outliers in Fig. 7d deviate significantly from Eq. (4). They occur in the GFDL model, mainly north of 45°N and south of 40°S (Fig. 4c), implying factors other than ΔnetSW and ΔLE, such as the energy redistribution factor, may also play a role in modifying ΔT.

An open question is whether Eq. (4) is a robust emergent relationship on subgrid variations under other CO_2 scenarios and on variations associated with other types of land use. To answer this question, we did three out-of-sample tests using the CESM2 model results (crop − psl in 4 × CO_2, grass − forest in SSP5–8.5 and crop − forest in SSP5-8.5; Table 1). We found that this relationship predicts ΔT reasonably well for the same subgrid tile configuration (crop vs psl) under 4 × CO_2 (Fig. 8a, $r = 0.92$), but does not work well for ΔT associated with two other tile configurations (grass vs forest, Fig. 8b; crop vs forest, Fig. 8c) under the SSP5-8.5 scenario. In these two cases, most of the data points lie above the regression line of Eq. (4). In the case of crop versus forest, the relationship is noisy with r value of 0.47 only. In other words, albedo and LE differences cannot fully explain the range of local temperature responses to LULCC.

Published modeling studies of large-scale deforestation have shown that the surface air temperature responds to changes in surface roughness in addition to changes in albedo and LE (e.g., Winckler et al. 2019b). In the local surface energy balance framework, this roughness effect can be quantified with the energy redistribution factor f (Lee et al. 2011). We analyzed the dependence of ΔT on various combinations of ΔnetSW, ΔLE, and Δf using a subset of the simulations with CESM2. We did not consider ΔnetSW − ΔLE − ΔH as

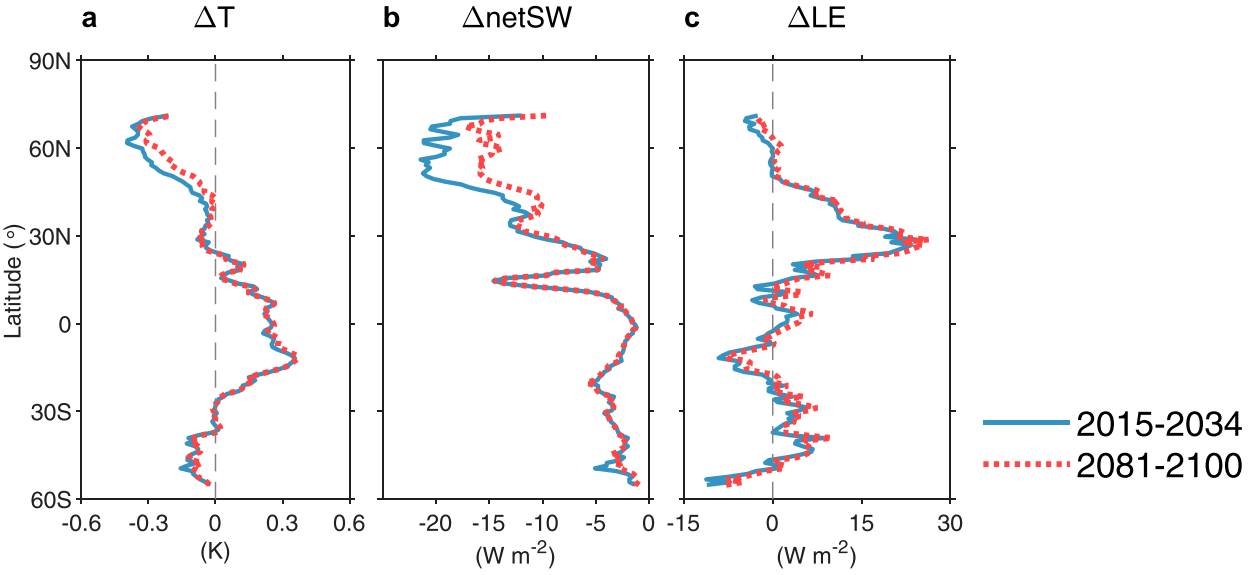

FIG. 6. Zonal mean differences (crop minus forest) of (a) temperature, (b) net SW radiation, and (c) LE flux under the SSP5–8.5 scenario in 2015–34 (blue) and 2081–2100 (red).

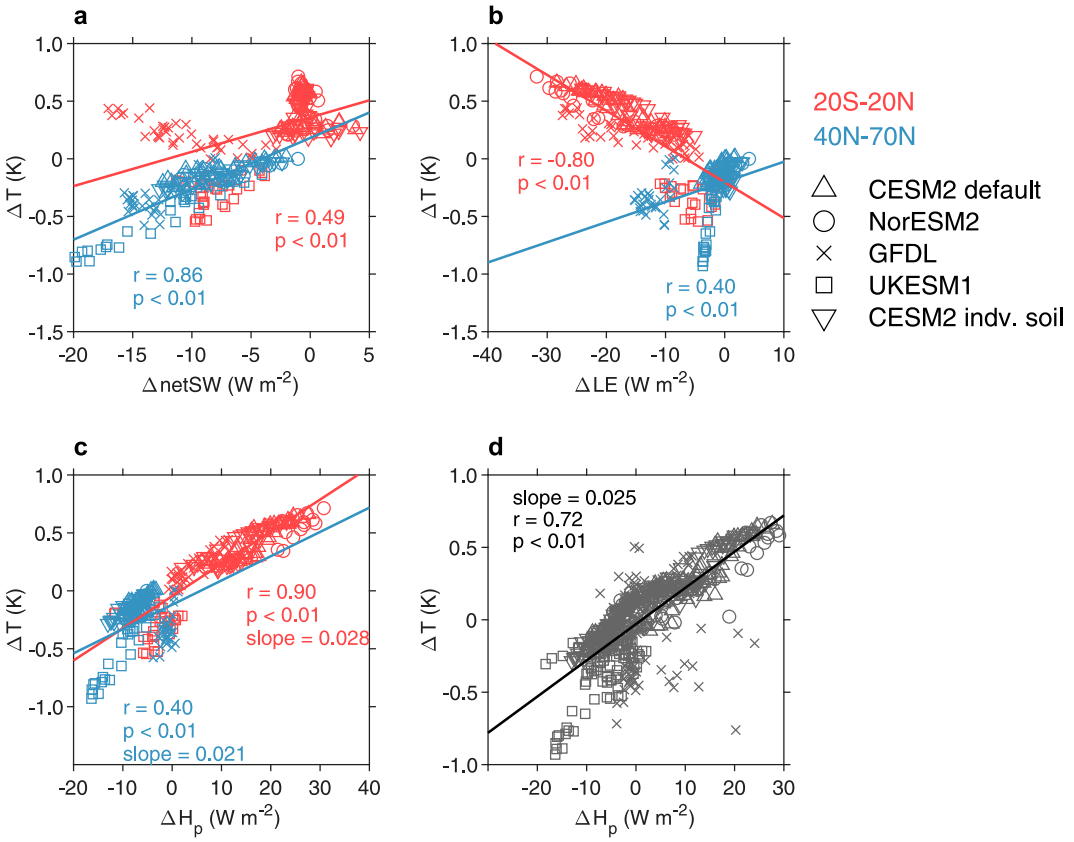

FIG. 7. Linear relationship between zonally averaged (a) ΔT and ΔnetSW, (b) ΔT and ΔLE, and (c),(d) ΔT and ΔH_p for all hist-noLu simulations (crop minus psl). In (a), (b), and (c), red and blue symbols represent tropics and mid–high-latitude regions, respectively. In (d), all latitude bands are used. Each symbol represents zonal mean value of one latitude band. The lines represent linear regression fit, with linear correlation (r) and confidence level (p) values shown.

predictor, because on the annual time scale this combination is roughly equivalent to Δ↑LW or change in the outgoing longwave radiation. Since ↑LW is controlled by the surface temperature according to the Stephan–Boltzmann law, use of Δ↑LW as a predictor of ΔT would amount to circular reasoning of explaining temperature with temperature. The best statistical model is obtained by regressing ΔT against ΔnetSW and Δf (all as zonal mean values):

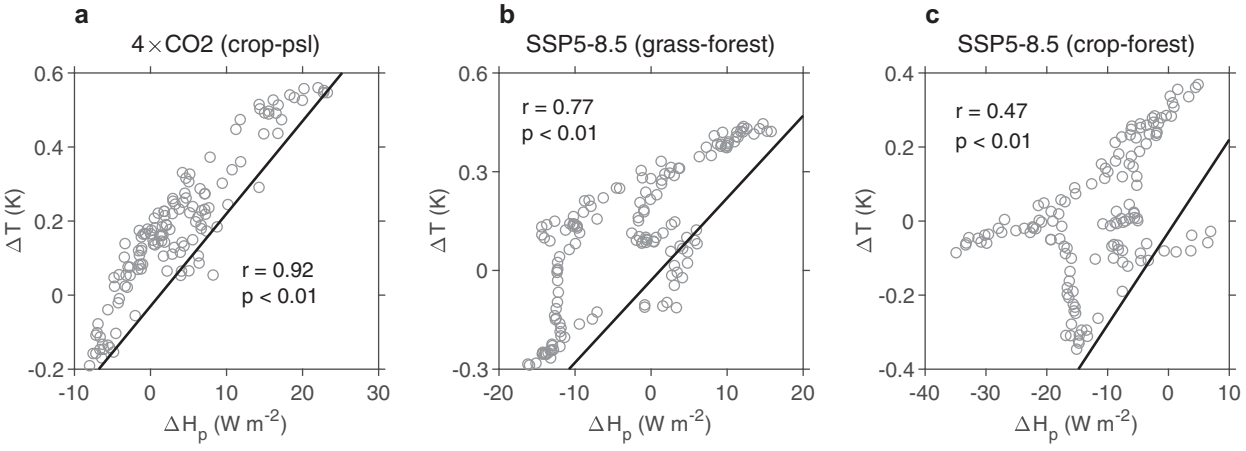

FIG. 8. Linear relationship between zonally averaged ΔT and ΔH_p for three out-of-sample tests of Eq. (4). Each symbol represents zonal mean value of one latitude band. The thick solid lines represent Eq. (4).

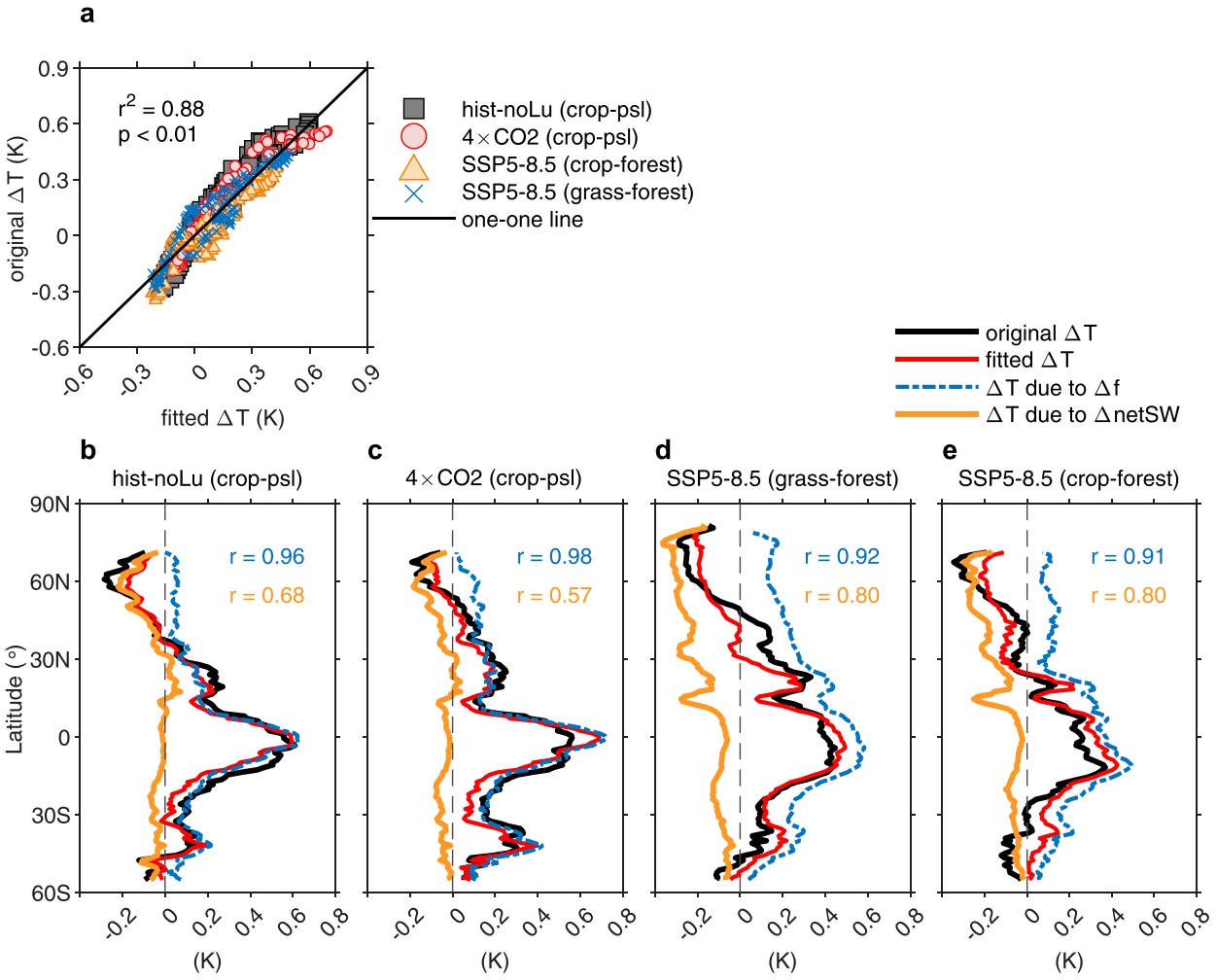

FIG. 9. An emergent relationship on subgrid temperature variations in CESM2 model simulations. (a) Original ΔT vs fitted ΔT [Eq. (5)]. (b)–(e) Zonal mean plot of original ΔT, fitted ΔT. In (b)–(e), the blue and orange lines represent contribution to ΔT from changes in energy redistribution factor and in netSW, respectively. The SSP5–8.5 results are for 2081–2100.

$$\Delta T = 0.017 \times \Delta\text{netSW} - 0.170 \times \Delta f - 0.018. \quad (5)$$

This linear model explains 88% of the variations ($r^2 = 0.88$) in ΔT between crop versus psl, crop versus forest, and grass versus forest under three different CO_2 forcing scenarios (historical, 4 × CO_2 and SSP5–8.5; Fig. 9a). Consistent with the heating potential relationship [Eqs. (1) and (4)], ΔT is positively related to ΔnetSW, indicating that land-use change that causes a reduction in albedo contributes to warming. On the other hand, the relationship with Δf is negative, or land-use change that increases the efficiency of surface-air energy redistribution contributes to cooling. The zonal patterns of Δf are given in Fig. S4. In these three tile pairs, open land tiles (crop and grass) have smaller f than their corresponding baseline tile (psl or forest). This is because f decreases with increasing heat diffusion resistance in the surface layer and with increasing Bowen ratio (Lee et al. 2011) and because open land tiles have higher diffusion resistance due to their lower roughness and generally higher Bowen ratio.

The individual contributions of ΔnetSW and Δf to ΔT can be estimated by multiplying their coefficients, respectively (Figs. 9b–e). In the three tile configurations, change in the energy redistribution factor dominates the latitudinal pattern of ΔT between 60°S and 30°N (blue lines). In mid–high latitudes (roughly north of 40°N), change in albedo is dominant, resulting in lower temperatures in open land (crop and grass) than in psl or forest.

f. Behavior of the UKESM1 model

In contrast to warming at low latitudes and cooling at high latitudes in the other model simulations, the UKESM1 model shows cooling due to cropland expansion across all latitudes (Figs. 1, 2 and 4). To understand this behavior, we compared the annual albedo and LE for the crop and the psl tile and their differences among the five hist-noLu

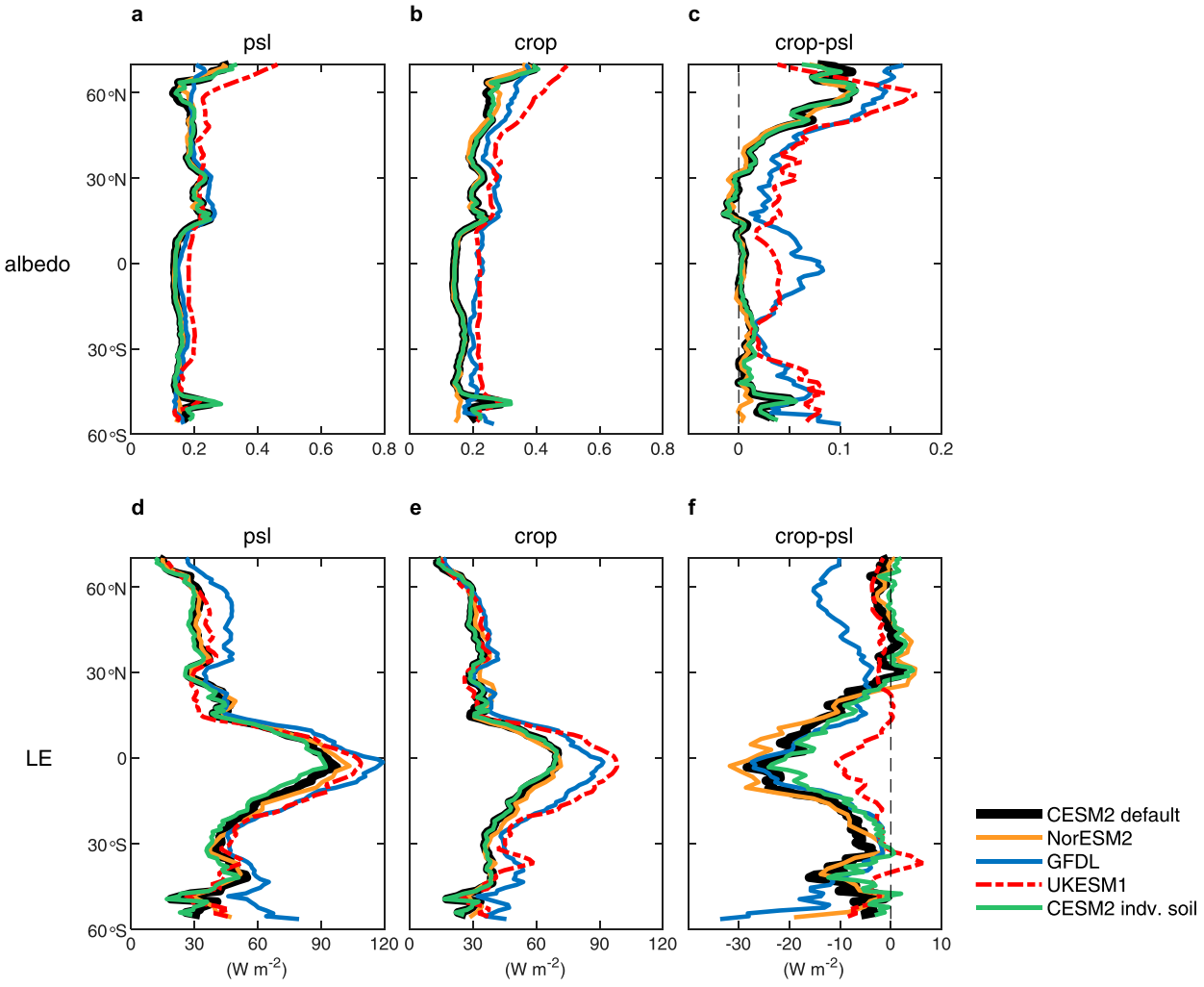

FIG. 10. Zonal mean plot of mean albedo in psl (a) tile, (b) crop land tile, and (c) their differences in hist-noLu simulations. (d)–(f) As in (a)–(c), but for LE flux.

model simulations (Fig. 10, Tables 2 and 3). The albedo of the crop tile in UKESM1 is generally higher than other models. In the region of 40°–70°N, the UKESM1 model has a mean crop albedo of 0.37 compared with 0.23 in CESM2 (default) and 0.29 in GFDL, causing a stronger reduction of net SW radiation (-13.8 W m^{-2}) than in other models (from -6.6 to -12.5 W m^{-2}). The most negative zonal mean ΔT of -0.93 K occurs in the UKESM1 simulation at 60°N (Fig. 4d).

The UKESM1 model shows a similar LE to CESM2 for the psl tile (Fig. 10d), but a roughly 20 W m^{-2} higher LE for the crop tile in the tropics relative to CESM2. This translates into a less negative LE change (-4.4 W m^{-2}) compared with CESM2 (-18.0 W m^{-2}) in the tropical region (Table 3), and

TABLE 2. Albedo and ΔnetSW radiation in each model for the tropics and mid–high latitudes.

	Mean albedo (psl)		Mean albedo (crop)		Δalbedo (crop − psl)		ΔnetSW (crop − psl; W m^{-2})	
Model	20°S–20°N	40°–70°N	20°S–20°N	40°–70°N	20°S–20°N	40°–70°N	20°S–20°N	40°–70°N
CESM2 default	0.16	0.19	0.16	0.23	0	0.04	−0.5	−6.6
NorESM2	0.16	0.19	0.16	0.24	0	0.05	−0.3	−6.6
GFDL	0.18	0.19	0.23	0.29	0.05	0.10	−10.4	−12.5
UKESM1	0.19	0.27	0.23	0.37	0.04	0.10	−8.1	−13.8
CESM2 individual soil	0.16	0.19	0.16	0.24	0	0.05	−0.4	−6.8

TABLE 3. LE flux in each model for the tropics and mid–high latitudes (W m^{-2}).

Model	Mean LE (psl)		Mean LE (crop)		ΔLE (crop − psl)	
	20°S–20°N	40°70°N	20°S–20°N	40°–70°N	20°S–20°N	40°–70°N
CESM2 default	72.1	30.4	54.2	29.7	−18.0	−0.8
NorESM2	75.4	31.2	54.5	31.5	−20.8	0.3
GFDL	85.6	44.3	70.2	32.8	−15.4	−11.6
UKESM1	77.7	31.8	73.3	29.1	−4.4	−2.7
CESM2 individual soil	68.5	28.5	54.0	29.4	−14.4	0.9

negative or near-zero ΔH_p (Fig. 4d) as opposed to large positive ΔH_P in CESM2 (Fig. 4a). The combination of a stronger albedo effect and a reduced LE change leads to the above-mentioned consistent cooling in UKESM1 model.

The GFDL model also shows a strong albedo-driven cooling effect at high latitudes and a high LE flux in the tropics for the crop tile (Figs. 10b,e). However, due to a high LE flux of the psl tile, the LE difference between crop and psl is similar to the other models at low latitudes and is negative at mid–high latitudes, which offsets the cooling effect from albedo.

5. Discussion and summary

In this study, we investigated the LULCC impact on local subgrid tile air temperature with a set of CMIP6 ESMs across a large range of CO_2 concentrations. We found that the subgrid temperature response to LULCC varies by latitude, and depends on the competing effects of albedo, LE and energy redistribution. Because of this balancing act, there exists a transitional latitude that divides warming to the south and cooling to the north from land clearing. Satellite-based studies on land surface temperature show that deforestation leads to cooling north of 45°–55°N (Alkama and Cescatti 2016; Duveiller et al. 2018), while in observational studies of air temperature, the transition from warming to cooling occurs farther south, at around 35°N (Lee et al. 2011; Zhang et al. 2014). In a model simulation of local deforestation (grass vs forest) under the historical climate (1991–2010; Schultz et al. 2016), the transition in air temperature change occurs at around 48°N. Winckler et al. (2019c) reported a transition of 45°–55°N for surface temperature in the MPI-ESM model. In the historical simulations presented here, the transition of positive ΔT (2-m air temperature, crop minus psl) to negative ΔT occurs at around 40°N (38°–42°N; Figs. 4a,b,c,e). The simulation of a transient climate scenario suggests that under future higher CO_2 conditions, the transition may shift farther north (Fig. 6a).

The latitudinal dependence of temperature response to LULCC can be further understood by quantifying the relative contribution of nonradiative processes. Following Bright et al. (2017), the nonradiative contribution is given as

$$\text{nonradiative fraction} = \frac{|\text{RH2}|}{(|\text{RH1}| + |\text{RH2}| + |\text{RH3}|)} \times 100\%. \quad (6)$$

In Eq. (6), |RH1|, |RH2|, and |RH3| are the first, second, and third terms on the right-hand side of Eq. (5). The zonal mean results (Fig. 11) show that the nonradiative contribution exceeds 50% between 45°S and 30°N, with peak values (>80%) at tropical latitudes (15°S and 10°N), over the ranges

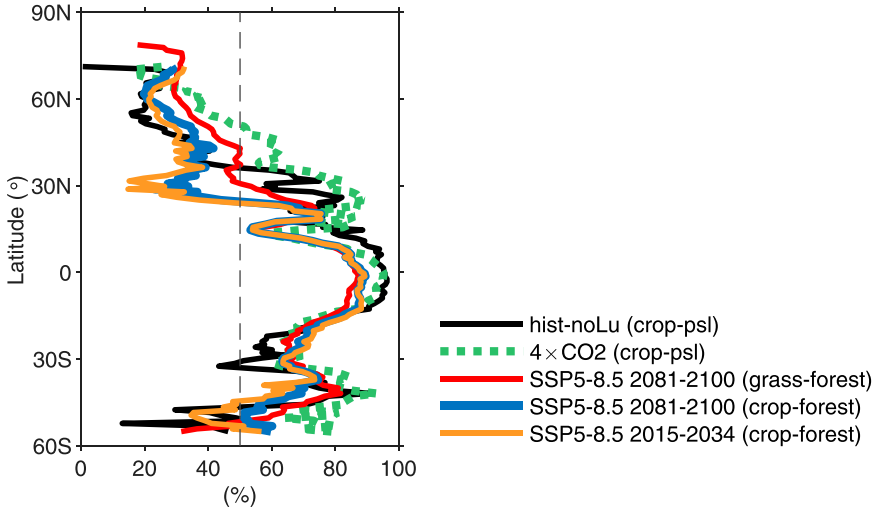

FIG. 11. Zonal mean fractions of ΔT contributed by nonradiative process in CESM2 simulations. Dashed line represents 50%.

of the CO_2 and land-use change scenarios simulated by CESM2. These results confirm the dominant role of nonradiative processes at these latitudes, consistent with previous analyses (Bright et al. 2017; Ge et al. 2019). For example, in Bright et al. (2017), the authors found that nonradiative processes dominate the local temperature response to LULCC effect, especially in the tropics. In more northern latitudes, the nonradiative contribution seems to be more sensitive to CO_2 concentration, irrigation status (the irrigation scheme was turned off in the $4 \times CO_2$ simulation) and LULCC type (Fig. 11).

Unlike the other models, the UKESM1 model shows cooling due to agricultural expansion across all latitudes (Fig. 4d). This different behavior arises largely from the higher albedo and the higher LE of the crop tile in UKESM1 than in the other models (Tables 2 and 3; Fig. 10). The land surface scheme in UKESM1 is JULES (Table 1). Previous modeling studies with JULES reveal that its albedo response to land clearing is too strong in comparison to other models (Kumar et al. 2013; Davies-Barnard et al. 2014; Robertson 2019; Winckler et al. 2019a). In an evaluation of JULES against an observational dataset, Robertson (2019) found that albedo errors in JULES are a major reason for its temperature biases. The exact cause of the albedo errors is not clear. It may be related to relative biases in optical parameter settings, such as leaf and soil albedo, among different PFTs or to LAI calculation and calculation of canopy radiation. They also suggest that errors in surface roughness length may partially explain its different LE response from other models. In these studies, performance evaluation is based on grid mean values in control versus perturbation simulations (Davies-Barnard et al. 2014), "all-forcing" simulations (Kumar et al. 2013) or "chessboard" simulations (Robertson 2019; Winckler et al. 2019a) as described in the introduction. Our analysis demonstrates similar parameterization biases at the subgrid level in JULES. This example supports the view that subgrid model data provides useful diagnostic information on land surface model performance.

The surface heating potential H_p has been used to explain the land surface temperature variations observed by satellites (Schultz et al. 2017). In the present study, H_p explains reasonably well the latitudinal dependence of the 2-m air temperature change between crop and psl land tiles for all the five hist-noLu model simulations (including UKESM1; $r = 0.72$, Eq. (4) and Fig. 7c). However, this relationship does not hold for two other subgrid tile configurations (grass vs forest; crop vs forest; Fig. 8). An alternative formulation, given by Eq. (5), combines the contributions to subgrid temperature variations from radiative processes via changes in the net SW radiation (primarily due to surface albedo change) and from nonradiative processes via the energy redistribution factor, the latter of which accounts for the surface roughness effect. Equation (5) appears more robust than the H_p relationship [Eq. (4)], explaining 88% of the subgrid air temperature variations between crop versus psl, crop versus forest, and grass versus forest tiles and under three different CO_2 forcing scenarios (historical, $4 \times CO_2$, and SSP5–8.5; Fig. 9a). In a pseudovalidation exercise, with the MODIS albedo product and CESM2-generated f values, we find that Eq. (5) fits reasonably well with the latitudinal variation of ΔT observed at 42 paired flux network (FLUXNET) sites [open land vs forest, values averaged every 5° of latitude; Lee et al. (2011) and Zhang et al. (2014); $r = 0.95$, $p < 0.001$, RMSE = 0.23 K; Fig. S5]. We suggest that Eq. (5) may serve as an emergent constraint for benchmarking the performance of land surface models and for prediction of local temperature response to LULCC.

One limitation of the present study is that atmospheric temperature data at the first model grid height (or blending height) are not available for three of the four ESMs. In keeping with the typical practice, these models archive air temperature at fixed pressure levels (1000, 925, 850 hPa, and so on), with the lowest level being 1000 hPa, or ~100 m above the sea level. However, the surface elevation in most land surface grids is greater than 100 m. Data at the blending height are necessary to perform diagnostic calculation of the energy redistribution factor f. Because of this data limitation, Eq. (5) is based on the data provided by CESM2 only. To check the robustness of Eq. (5), we also estimated the f values for the four hist-noLu simulations (CESM2 default, NorESM2, GFDL, UKESM1; Table 1), using the temperature at the lowest pressure level as a substitute for the blending height temperature. Using the Δf value obtained this way along with ΔnetSW, we calculated the ΔT from Eq. (5). The results, presented in Fig. S6, show that Eq. (5) performs reasonably well across the four ESM models. As f is increasingly used in LULCC studies, it is imperative that in future LUMIP-like projects, outputs for the blending height be archived along with surface and 2-m height variables.

In summary, our study shows that the albedo effect and LE flux response cannot fully explain the temperature response to LULCC activities. A new emergent relationship is proposed that combines the albedo effect and the effect of energy redistribution between the surface and the atmosphere. This relationship highlights the dominant role of nonradiative processes in the temperature response. Simulations under higher CO_2 conditions indicate that rising atmospheric CO_2 can alter the local climate effects of LULCC indirectly by altering irrigation intensity and snow cover duration. These insights from a multimodel and multiscenario perspective may be helpful to evaluate the performance of land surface model parameterizations.

Acknowledgments. We acknowledge the support from the U.S. National Science Foundation (Grant AGS1933630 to X.L.). High-performance computing support from Cheyenne (https://doi.org/10.5065/D6RX99HX) was provided by the NCAR's Computational and Information System Laboratory, sponsored by the National Science Foundation and other agencies. D.M.L. is supported by the National Center for Atmospheric Research, which is a major facility sponsored by the NSF under Cooperative Agreement 1852977 and by the U.S. Department of Energy, Office of Biological and Environmental Research Grant DE-FC03-97ER62402/A0101.

Data availability statement. The CMIP6/LUMIP model output used in this study is available at https://esgf-node.llnl.

gov/projects/cmip6/. The output of the SSP5–8.5 simulation is available at https://doi.org/10.7910/DVN/HUXAH6. The output of the 4 × CO_2 simulation, the data and Matlab scripts used in figure production are available upon reasonable request.

REFERENCES

Alkama, R., and A. Cescatti, 2016: Biophysical climate impacts of recent changes in global forest cover. *Science*, **351**, 600–604, https://doi.org/10.1126/science.aac8083.

Bonan, G. B., 2001: Observational evidence for reduction of daily maximum temperature by croplands in the Midwest United States. *J. Climate*, **14**, 2430–2442, https://doi.org/10.1175/1520-0442(2001)014<2430:OEFROD>2.0.CO;2.

——, 2008: Forests and climate change: Forcings, feedbacks, and the climate benefits of forests. *Science*, **320**, 1444–1449, https://doi.org/10.1126/science.1155121.

——, D. Pollard, and S. L. Thompson, 1992: Effects of boreal forest vegetation on global climate. *Nature*, **359**, 716–718, https://doi.org/10.1038/359716a0.

Boysen, L. R., and Coauthors, 2020: Global climate response to idealized deforestation in CMIP6 models. *Biogeosciences*, **17**, 5615–5638, https://doi.org/10.5194/bg-17-5615-2020.

Bright, R. M., E. Davin, T. O'Halloran, J. Pongratz, K. Zhao, and A. Cescatti, 2017: Local temperature response to land cover and management change driven by non-radiative processes. *Nat. Climate Change*, **7**, 296–302, https://doi.org/10.1038/nclimate3250.

Chakraborty, T., and X. Lee, 2019: Land cover regulates the spatial variability of temperature response to the direct radiative effect of aerosols. *Geophys. Res. Lett.*, **46**, 8995–9003, https://doi.org/10.1029/2019GL083812.

Chen, L., and P. A. Dirmeyer, 2020: Reconciling the disagreement between observed and simulated temperature responses to deforestation. *Nat. Commun.*, **11**, 202, https://doi.org/10.1038/s41467-019-14017-0.

Danabasoglu, G., and Coauthors, 2020: The Community Earth System Model version 2 (CESM2). *J. Adv. Model. Earth Syst.*, **12**, e2019MS001916, https://doi.org/10.1029/2019MS001916.

da Rocha, H. R., M. L. Goulden, S. D. Miller, M. C. Menton, L. D. V. O. Pinto, H. C. de Freitas, and A. M. Silva Figueira, 2004: Seasonality of water and heat fluxes over a tropical forest in eastern Amazonia. *Ecol. Appl.*, **14**, 22–32, https://doi.org/10.1890/02-6001.

Davies-Barnard, T., P. J. Valdes, J. S. Singarayer, and C. D. Jones, 2014: Climatic impacts of land-use change due to crop yield increases and a universal carbon tax from a scenario model. *J. Climate*, **27**, 1413–1424, https://doi.org/10.1175/JCLI-D-13-00154.1.

Davin, E. L., and N. de Noblet-Ducoudré, 2010: Climatic impact of global-scale deforestation: Radiative versus nonradiative processes. *J. Climate*, **23**, 97–112, https://doi.org/10.1175/2009JCLI3102.1.

Dunne, J. P., and Coauthors, 2020: The GFDL Earth System Model version 4.1 (GFDL-ESM4): Overall coupled model description and simulation characteristics. *J. Adv. Model. Earth Syst.*, **12**, e2019MS002015, https://doi.org/10.1029/2019MS002015.

Duveiller, G., J. Hooker, and A. Cescatti, 2018: The mark of vegetation change on Earth's surface energy balance. *Nat. Commun.*, **9**, 679, https://doi.org/10.1038/s41467-017-02810-8.

Eyring, V., S. Bony, G. A. Meehl, C. A. Senior, B. Stevens, R. J. Stouffer, and K. E. Taylor, 2016: Overview of the Coupled Model Intercomparison Project Phase 6 (CMIP6) experimental design and organization. *Geosci. Model Dev.*, **9**, 1937–1958, https://doi.org/10.5194/gmd-9-1937-2016.

Findell, K. L., A. Berg, P. Gentine, J. P. Krasting, B. R. Lintner, S. Malyshev, J. A. Santanello, and E. Shevliakova, 2017: The impact of anthropogenic land use and land cover change on regional climate extremes. *Nat. Commun.*, **8**, 989, https://doi.org/10.1038/s41467-017-01038-w.

Ge, J., W. Guo, A. J. Pitman, M. G. De Kauwe, X. Chen, and C. Fu, 2019: The nonradiative effect dominates local surface temperature change caused by afforestation in China. *J. Climate*, **32**, 4445–4471, https://doi.org/10.1175/JCLI-D-18-0772.1.

Hall, A., P. Cox, C. Huntingford, and S. Klein, 2019: Progressing emergent constraints on future climate change. *Nat. Climate Change*, **9**, 269–278, https://doi.org/10.1038/s41558-019-0436-6.

Hao, D., and Coauthors, 2022: Impacts of sub-grid topographic representations on surface energy balance and boundary conditions in the E3SM land model: A case study in Sierra Nevada. *J. Adv. Model. Earth Syst.*, **14**, e2021MS002862, https://doi.org/10.1029/2021MS002862.

Hurtt, G. C., and Coauthors, 2020: Harmonization of global land use change and management for the period 850–2100 (LUH2) for CMIP6. *Geosci. Model Dev.*, **13**, 5425–5464, https://doi.org/10.5194/gmd-13-5425-2020.

Jia, G., and Coauthors, 2019: Land–climate interactions. *Climate Change and Land*, P. R. Shukla et al., Eds., Cambridge University Press, 131–247.

Kumar, S., P. A. Dirmeyer, V. Merwade, T. DelSole, J. M. Adams, and D. Niyogi, 2013: Land use/cover change impacts in CMIP5 climate simulations: A new methodology and 21st century challenges. *J. Geophys. Res. Atmos.*, **118**, 6337–6353, https://doi.org/10.1002/jgrd.50463.

Lamchin, M., and Coauthors, 2020: Understanding global spatio-temporal trends and the relationship between vegetation greenness and climate factors by land cover during 1982–2014. *Global Ecol. Conserv.*, **24**, e01299, https://doi.org/10.1016/j.gecco.2020.e01299.

Lawrence, D., and K. Vandecar, 2015: Effects of tropical deforestation on climate and agriculture. *Nat. Climate Change*, **5**, 27–36, https://doi.org/10.1038/nclimate2430.

Lawrence, D. M., and Coauthors, 2016: The Land Use Model Intercomparison Project (LUMIP) contribution to CMIP6: Rationale and experimental design. *Geosci. Model Dev.*, **9**, 2973–2998, https://doi.org/10.5194/gmd-9-2973-2016.

——, and Coauthors, 2018: Technical description of version 5.0 of the Community Land Model (CLM). NCAR Tech. Note, 337 pp., https://www.cesm.ucar.edu/models/cesm2/land/CLM50_Tech_Note.pdf.

——, and Coauthors, 2019: The Community Land Model version 5: Description of new features, benchmarking, and impact of forcing uncertainty. *J. Adv. Model. Earth Syst.*, **11**, 4245–4287, https://doi.org/10.1029/2018MS001583.

Lee, X., and Coauthors, 2011: Observed increase in local cooling effect of deforestation at higher latitudes. *Nature*, **479**, 384–387, https://doi.org/10.1038/nature10588.

Lejeune, Q., S. I. Seneviratne, and E. L. Davin, 2017: Historical land-cover change impacts on climate: Comparative assessment of LUCID and CMIP5 multimodel experiments. *J. Climate*, **30**, 1439–1459, https://doi.org/10.1175/JCLI-D-16-0213.1.

Li, D., S. Malyshev, and E. Shevliakova, 2016: Exploring historical and future urban climate in the Earth System Modeling

framework: 1. Model development and evaluation. *J. Adv. Model. Earth Syst.*, **8**, 917–935, https://doi.org/10.1002/2015MS000578.

Li, Y., M. Zhao, S. Motesharrei, Q. Mu, E. Kalnay, and S. Li, 2015: Local cooling and warming effects of forests based on satellite observations. *Nat. Commun.*, **6**, 6603, https://doi.org/10.1038/ncomms7603.

——, N. De Noblet-Ducoudré, E. L. Davin, S. Motesharrei, N. Zeng, S. Li, and E. Kalnay, 2016a: The role of spatial scale and background climate in the latitudinal temperature response to deforestation. *Earth Syst. Dyn.*, **7**, 167–181, https://doi.org/10.5194/esd-7-167-2016.

——, and Coauthors, 2016b: Potential and actual impacts of deforestation and afforestation on land surface temperature. *J. Geophys. Res. Atmos.*, **121**, 14 372–314 386, https://doi.org/10.1002/2016JD024969.

Liao, W., X. Liu, E. Burakowski, D. Wang, L. Wang, and D. Li, 2020: Sensitivities and responses of land surface temperature to deforestation-induced biophysical changes in two global Earth system models. *J. Climate*, **33**, 8381–8399, https://doi.org/10.1175/JCLI-D-19-0725.1.

Malyshev, S., E. Shevliakova, R. J. Stouffer, and S. W. Pacala, 2015: Contrasting local versus regional effects of land-use-change-induced heterogeneity on historical climate: Analysis with the GFDL Earth System Model. *J. Climate*, **28**, 5448–5469, https://doi.org/10.1175/JCLI-D-14-00586.1.

Meier, R., and Coauthors, 2018: Evaluating and improving the Community Land Model's sensitivity to land cover. *Biogeosciences*, **15**, 4731–4757, https://doi.org/10.5194/bg-15-4731-2018.

Meinshausen, M., and Coauthors, 2020: The Shared Socioeconomic Pathway (SSP) greenhouse gas concentrations and their extensions to 2500. *Geosci. Model Dev.*, **13**, 3571–3605, https://doi.org/10.5194/gmd-13-3571-2020.

Oleson, K. W., A. Monaghan, O. Wilhelmi, M. Barlage, N. Brunsell, J. Feddema, L. Hu, and D. F. Steinhoff, 2015: Interactions between urbanization, heat stress, and climate change. *Climatic Change*, **129**, 525–541, https://doi.org/10.1007/s10584-013-0936-8.

Pan, Y., and Coauthors, 2011: A large and persistent carbon sink in the world's forests. *Science*, **333**, 988–993, https://doi.org/10.1126/science.1201609.

Paulot, F., S. Malyshev, T. Nguyen, J. D. Crounse, E. Shevliakova, and L. W. Horowitz, 2018: Representing sub-grid scale variations in nitrogen deposition associated with land use in a global Earth system model: Implications for present and future nitrogen deposition fluxes over North America. *Atmos. Chem. Phys.*, **18**, 17 963–17 978, https://doi.org/10.5194/acp-18-17963-2018.

Pielke, R. A., Sr., and Coauthors, 2011: Land use/land cover changes and climate: Modeling analysis and observational evidence. *Wiley Interdiscip. Rev.: Climate Change*, **2**, 828–850, https://doi.org/10.1002/wcc.144.

Pitman, A. J., and Coauthors, 2009: Uncertainties in climate responses to past land cover change: First results from the lucid intercomparison study. *Geophys. Res. Lett.*, **36**, L14814, https://doi.org/10.1029/2009GL039076.

Prevedello, J. A., G. R. Winck, M. M. Weber, E. Nichols, and B. Sinervo, 2019: Impacts of forestation and deforestation on local temperature across the globe. *PLOS ONE*, **14**, e0213368, https://doi.org/10.1371/journal.pone.0213368.

Ren, X., M. Weitzel, B. C. O'Neill, P. Lawrence, P. Meiyappan, S. Levis, E. J. Balistreri, and M. Dalton, 2018: Avoided economic impacts of climate change on agriculture: Integrating a land surface model (CLM) with a global economic model (iPETS). *Climatic Change*, **146**, 517–531, https://doi.org/10.1007/s10584-016-1791-1.

Robertson, E., 2019: The local biophysical response to land-use change in HadGEM2-ES. *J. Climate*, **32**, 7611–7627, https://doi.org/10.1175/JCLI-D-18-0738.1.

Robinson, D. A., and G. Kukla, 1984: Albedo of a dissipating snow cover. *J. Appl. Meteor. Climatol.*, **23**, 1626–1634, https://doi.org/10.1175/1520-0450(1984)023<1626:AOADSC>2.0.CO;2.

Schultz, N. M., X. Lee, P. J. Lawrence, D. M. Lawrence, and L. Zhao, 2016: Assessing the use of subgrid land model output to study impacts of land cover change. *J. Geophys. Res. Atmos.*, **121**, 6133–6147, https://doi.org/10.1002/2016JD025094.

——, P. J. Lawrence, and X. Lee, 2017: Global satellite data highlights the diurnal asymmetry of the surface temperature response to deforestation. *J. Geophys. Res. Biogeosci.*, **122**, 903–917, https://doi.org/10.1002/2016JG003653.

Seland, Ø., and Coauthors, 2020: Overview of the Norwegian Earth System Model (NorESM2) and key climate response of CMIP6 DECK, historical, and scenario simulations. *Geosci. Model Dev.*, **13**, 6165–6200, https://doi.org/10.5194/gmd-13-6165-2020.

Sellar, A. A., and Coauthors, 2019: UKESM11: Description and evaluation of the UK Earth System Model. *J. Adv. Model. Earth Syst.*, **11**, 4513–4558, https://doi.org/10.1029/2019MS001739.

Shevliakova, E., and Coauthors, 2009: Carbon cycling under 300 years of land use change: Importance of the secondary vegetation sink. *Global Biogeochem. Cycles*, **23**, GB2022, https://doi.org/10.1029/2007GB003176.

Taylor, K. E., R. J. Stouffer, and G. A. Meehl, 2012: An overview of CMIP5 and the experiment design. *Bull. Amer. Meteor. Soc.*, **93**, 485–498, https://doi.org/10.1175/BAMS-D-11-00094.1.

Tesfa, T. K., and L.-Y. R. Leung, 2017: Exploring new topography-based subgrid spatial structures for improving land surface modeling. *Geosci. Model Dev.*, **10**, 873–888, https://doi.org/10.5194/gmd-10-873-2017.

von Randow, C., and Coauthors, 2004: Comparative measurements and seasonal variations in energy and carbon exchange over forest and pasture in south west Amazonia. *Theor. Appl. Climatol.*, **78**, 5–26, https://doi.org/10.1007/s00704-004-0041-z.

Wang, W., X. H. Lee, W. Xiao, S. D. Liu, N. Schultz, Y. W. Wang, M. Zhang, and L. Zhao, 2018: Global lake evaporation accelerated by changes in surface energy allocation in a warmer climate. *Nat. Geosci.*, **11**, 410–414, https://doi.org/10.1038/s41561-018-0114-8.

Wiltshire, A. J., and Coauthors, 2020: JULES-GL7: The Global Land configuration of the Joint UK Land Environment Simulator version 7.0 and 7.2. *Geosci. Model Dev.*, **13**, 483–505, https://doi.org/10.5194/gmd-13-483-2020.

Winckler, J., C. H. Reick, and J. Pongratz, 2017: Robust identification of local biogeophysical effects of land-cover change in a global climate model. *J. Climate*, **30**, 1159–1176, https://doi.org/10.1175/JCLI-D-16-0067.1.

——, Q. Lejeune, C. H. Reick, and J. Pongratz, 2019a: Nonlocal effects dominate the global mean surface temperature response to the biogeophysical effects of deforestation. *Geophys. Res. Lett.*, **46**, 745–755, https://doi.org/10.1029/2018GL080211.

——, C. H. Reick, R. M. Bright, and J. Pongratz, 2019b: Importance of surface roughness for the local biogeophysical effects of deforestation. *J. Geophys. Res. Atmos.*, **124**, 8605–8618, https://doi.org/10.1029/2018JD030127.

——, and Coauthors, 2019c: Different response of surface temperature and air temperature to deforestation in climate models. *Earth Syst. Dyn.*, **10**, 473–484, https://doi.org/10.5194/esd-10-473-2019.

Yang, Y., M. L. Roderick, S. Zhang, T. R. McVicar, and R. J. Donohue, 2019: Hydrologic implications of vegetation response to elevated CO_2 in climate projections. *Nat. Climate Change*, **9**, 44–48, https://doi.org/10.1038/s41558-018-0361-0.

Zhang, K., and Coauthors, 2022: A global dataset on subgrid land surface climate (2015–2100) from the Community Earth System Model. *Geosci. Data J.*, https://doi.org/10.1002/gdj3.153, in press.

Zhang, M., and Coauthors, 2014: Response of surface air temperature to small-scale land clearing across latitudes. *Environ. Res. Lett.*, **9**, 034002, https://doi.org/10.1088/1748-9326/9/3/034002.

Zhao, L., X. Lee, R. B. Smith, and K. Oleson, 2014: Strong contributions of local background climate to urban heat islands. *Nature*, **511**, 216–219, https://doi.org/10.1038/nature13462.

Zhao, M., and Coauthors, 2018: The GFDL Global Atmosphere and Land Model AM4.0/LM4.0: 2. Model description, sensitivity studies, and tuning strategies. *J. Adv. Model. Earth Syst.*, **10**, 735–769, https://doi.org/10.1002/2017MS001209.